

## **Chapter 3:**

### **Growth dynamics and characterization techniques**

### 3.1. Thin film growth

In physical vapor deposition method, thin films are formed when the depositing materials condensed on the surface of the substrate from its vapor phase. Various growth dynamical processes and thermodynamics are typically involved in the production of a good quality continuous film. A brief overview of these processes is given in the following sections.

#### 3.1.1. Surface diffusion

During the conversion process from vapor to condense state on the substrate the atom's kinetic energy is mainly distributed in the form of lattice vibration. The surface atoms create a potential energy distribution for the adatoms, fluctuations of which in turn make some adsorption sites more energetically preferable than others. Furthermore, adatoms having sufficient energy to overcome the energy barrier for the surface diffusion can move through such preferential positions. This process is called surface diffusion. The two-dimensional random walk problem can describe the surface diffusion process quite well. The rate of this process is usually expressed as a function of adatom jump rate ( $v$ ) which is given as [1]

$$v = v_0 \exp\left(-\frac{E_D}{kT}\right) \quad (3.1)$$

where,  $v_0$ ,  $k$ ,  $T$ , and  $E_D$  are the attempt frequency, Boltzmann constant, deposition temperature and energy of the barrier on the growth surface, respectively. The adatoms' diffusion coefficient ( $D$ ) can be expressed by a mathematical relation as follows [1]

$$D = \frac{1}{4} a^2 v = \frac{1}{4} a^2 v_0 \exp\left(-\frac{E_D}{kT}\right) \quad (3.2)$$

here,  $a$  is the distance moved in each step. Factor  $\frac{1}{4}$  in the above equation arises due to the two-dimensional diffusion of adatoms along the surface. The atomic interaction between adatom and substrate and surface morphology are the additional factors that determine the value of  $E_D$ , as shown in Figure 3.1 (a). Adatoms on the top surface can only experience  $E_D$ , at the time of diffusion between two adjacent sites. However, for going down along a step, a large amount of energy is required to break the bond which thereby producing another barrier called the Ehrlich-Schwoebel barrier ( $E_{ES}$ ) (Figure 3.1 (b)). Moreover, a high coordination number associated with the ascending step edges makes them energetically more stable. The diffusion of the adatom on the surface increases with increasing deposition temperature (equation 3.2). However, at low temperatures, the impingement of the adatoms at grazing incidence makes the

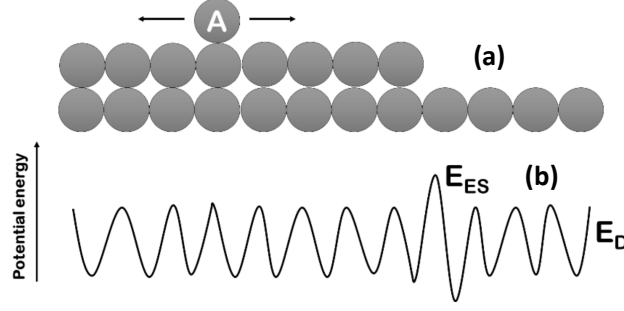


Figure 3.1. (a) The possible diffusion direction of an adatom on the top surface. (b) The potential distribution with two energy barriers  $E_{ES}$  and  $E_D$ .

the value of diffusion length very high [2, 3]. In this case, diffusion takes place along the direction of the adatoms' momentum component along the surface [4].

### 3.1.2. Nucleation

There are chances of two distinct possibilities when the adatoms reached the atomically flat surface. The adatoms either desorb back to the vapor phase or diffuse unless forming bonds with other strongly bounded adatoms. This leads to the formation of the cluster with different sizes. The cluster with size greater than a critical value ( $i^*$ ) can only form a stable nucleus otherwise they again come back to form two-dimensional adatom gas. Usually, the value of  $i^*$  is determined in terms of the number of atoms. The value of  $i^*$  is unity [5] when the cluster formation probability is quite higher than the dissociation, which is usually observed during low-temperature growth.

Typically, the nucleation process is expressed in terms of the number of atomic islands per unit area, also called the island density ( $N$ ). The quantity of the evaporant/precursors initially decides the value of  $N$  [1]. This is known as the transient nucleation regime and is valid until an appreciable amount of diffusing adatoms are captured by already existing islands. Under this situation,  $N$  approximately becomes [1]

$$N \sim (F_{avg}/D)^x. \quad (3.3)$$

Here,  $F_{avg}$  and  $x$  are the average deposition rate and scaling exponent, respectively. We have assumed that the atoms are continuously arriving from the vapor phase. The value of  $N$  can be easily increased by growing at a lower temperature. During the formation of three-dimensional islands on a two-dimensional surface,  $x$  becomes [1]

$$x = \frac{i^*}{i^* + 2.5} \quad (3.4)$$

It is worthwhile to mention that the nucleation mechanism can be modified by continuously chopping the impinging vapor flux. The adatoms' lifetime ( $\tau_m$ ) usually approximated as [6]

$$\tau_m \approx \frac{l^2}{D} \quad (3.5)$$

when the incident adatoms diffuse to the existing islands having a mean separation of  $2l$ . For  $\tau_m \gg 1/f$ , where  $f$  is the frequency of chopping, all adatoms are not able to diffuse into the existing island till the reaching of the next pulse. Consequently, the substrate constantly experiences an average deposition flux of  $F_i t_{on} f$ , where  $F_i$  is the amplitude and  $t_{on}$  is the width of the pulse. On the other hand, for  $\tau_m \ll t_{on}$ , adatoms nucleate as soon as they appear. Finally, in the case of  $t_{on} < \tau_m < 1/f$ , adatoms diffusion takes place although all of them disappear before the arrival of the next pulse.

### 3.1.3. Coalescence processes

#### 3.1.3.1. Ostwald ripening

The nucleation of adatoms on the growing surface creates islands with different sizes. However, the large islands are energetically more stable than the small ones [7] which possess higher apparent solubility. Thus, the adatoms accumulate to the larger island leaving the smaller ones. In 2007 International union of pure and applied chemistry (IUPAC) has mentioned the Ostwald ripening as “dissolution of small crystals or sol particles and the re-deposition of the dissolved species on the surface of larger crystals or sol particles”. However, this process only takes place in the presence of low adatomic super-saturation which is rare in thin-film growth [8]. A pictorial representation of this process is shown in Figure 3.2.

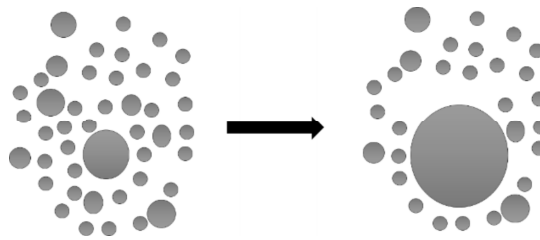


*Figure 3.2. A pictorial representation of Ostwald ripening where bigger crystallites are formed in expenses of smaller ones*

#### 3.1.3.2. Sintering

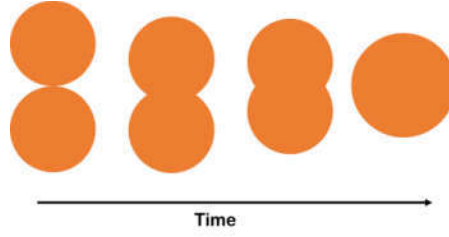


Figure 3.3. Schematic illustration of two islands during coalescing.

The size of the islands increases with time during growth by capturing atoms from the vapor. As a result, the separation between such islands reduces and they merge to form a single island to minimize the energy. A schematic illustration of this process is displayed in Figure 3.3. The time taken by two spherical/hemispherical islands of radius  $R$ , for completion of the coalescence ( $\tau_{coal}$ ) is written below [9, 10]

$$\tau_{coal} = \frac{R^4}{B} \quad (3.6)$$

here  $B$  is a coalescence parameter that depends on the material and temperature of the deposition. [9, 10]

$$B = \frac{D_s \gamma \Omega^2 S_0}{k_B T} \quad (3.7)$$

where  $D_s$ ,  $\gamma$ ,  $\Omega$  and  $S_0$  are the diffusion coefficient, surface energy, atomic volume and the number of diffusing atoms per unit surface area. The grain boundary usually arises due to the non-identical crystallographic orientation of two different islands. For completion of the coalescence process, the grain boundary must have disappeared [10].

### 3.1.3.3. Cluster migration

Another possibility that unlike the Ostwald ripening process, sometimes entire small islands acquire sufficient mobility to migrate through the surface and unified with the large ones. The diffusivity of the islands is inversely related to their sizes. Islands with less than ten atoms are usually favorable for cluster migration. However, in some situations, this procedure is even observed for island comprising of hundreds of atoms [11].

### 3.1.4. Continuous film formation

According to equation (3.6), the coalescence rate increases with increasing the size of the islands. Therefore, at a certain time of deposition, the island becomes sufficiently large, as a result, the formation of the next island starts without completion of the previous one. The

elongated islands are separated by voids on the surface. A large number of these structures joining together to make a network of correlated islands. Thereafter, the adatoms diffuse which in turn fills up the voids to form a continuous film.

### 3.2. Growth evolution

The formation of a continuous film can be possible following different paths. This is due to the film-substrate interaction and growth condition. As a consequence of different growth process, leads to the forming of different microstructures and morphologies. More explanations regarding the film growth are presented in the following section.

#### 3.2.1. Thermodynamic considerations

Thermodynamical consequences on microstructural evolution in epitaxial growth are determined by relating three different surface energy of the substrate ( $\gamma_s$ ), the film ( $\gamma_f$ ) and the film-substrate interface ( $\gamma_i$ ). Usually, in epitaxial growth,  $\gamma_s \geq \gamma_f + \gamma_i$ , which states that in order to minimize the surface energy the film entirely wets the substrate. Thus, the film grows in a layer by layer fashion which is known as the Frank van der Merwe growth mode as illustrated

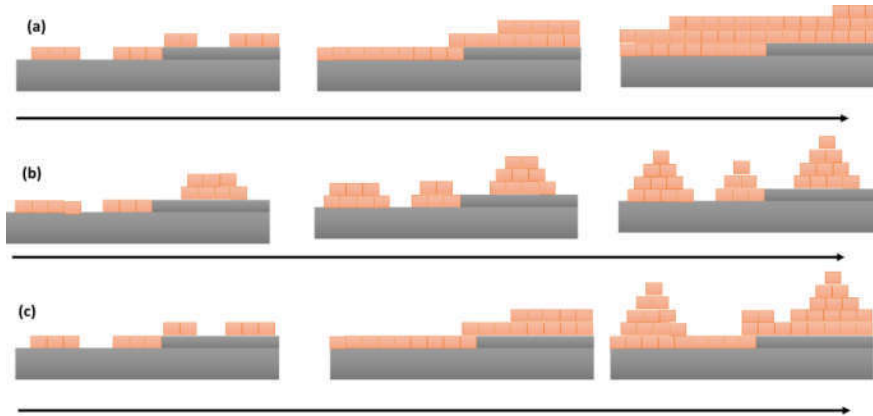


Figure 3.4. Illustration of different growth modes depending on the surface energies. (a) Frank van der Merwe (layer-by-layer), (b) Volmer-Weber (island formation) and (c) Stranski-Krastanov (layer-plus-island) growth mode.

in Figure (3.4 (a)). In the case of homoepitaxy,  $\gamma_i$  becomes zero [12]. However, if  $\gamma_s < \gamma_f + \gamma_i$  the surface energy is still minimized by bunching up and growing more islands during deposition. This is known as the Volmer-Weber growth mode, depicted in Figure (3.4 (b)). Another growth mode with layer by layer fashion also exists up to a critical thickness above which the relaxation of strain forms three-dimensional islands. This is well known as the Stranski-Krastanov growth mode shown in Figure (3.4 (c)).

#### 3.2.2. Kinetic considerations

It is well known that in the PVD process, the deposition of thin films often takes place without reaching the thermodynamic equilibrium, which means the growth kinetics also affects the deposition mechanism. This situation can be explained by employing the concept of two different diffusion barriers  $E_D$  and  $E_{ES}$ . If the adatom having sufficient energy to overcome both the barrier ( $E_D$  and  $E_{ES}$ ) and diffusion length is larger compared to the terrace width, they move down the steps and get accumulated at the edges. It is called step flow growth (Figure 3.5 (a)). In case of high enough diffusivity to overcome the diffusion barrier with shorter diffusion length with respect to terrace width, the two-dimensional island formed on the top

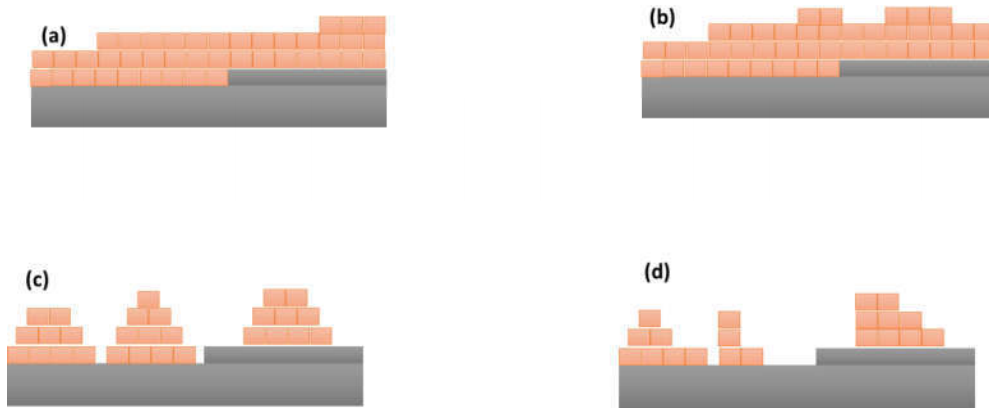


Figure 3.5. Graphical representation of different growth processes (a) step flow growth (b) layer-by-layer growth (c) kinetic roughening (d) self-affine growth.

layer. In this process, new nucleation could not begin unless the formation of a layer completes. Thus, resulting in a layer-by-layer growth (Figure 3.5 (b)). When the interlayer adatoms diffusion does not occur owing to high  $E_{ES}$ , they accumulate and form three dimensional heap as illustrated in Figure 3.5 (c). Finally, the adatoms having energy less than the  $E_D$  are unable to diffuse through the surface. Thus, they simply stick to the point of incidence. It is called self-affine growth which produces high surface roughness (Figure 3.5 (d)).

### 3.3. Off-normal film growth

In a three-dimensional growth procedure after the formation of a continuous film (Volmer-Weber type growth) each grain develops along the substrate normal since more atoms are supplied from the vapor. As a result, columnar microstructures formed with columns separated by grain boundaries as depicted in Figure 3.6 (a). In case oblique incidence of the flux with respect to the normal of the surface, initially formed islands obstruct the area behind them which inhibits the growth of those regions. Hence, the columns are isolated from each other and directed towards the source shown in Figure 3.6 (b). The amount of inclination of the column depends on the incidence angle of the vapor flux, which can be altered by several

factors like changing film composition [13], the spatial distribution of the vapor flux [14-16] or the kinetic growth conditions [17-21]. Using highly ionized vapor fluxes is another way to change the column inclination [22]. The higher ionization degree makes the column closer to the substrate normal.

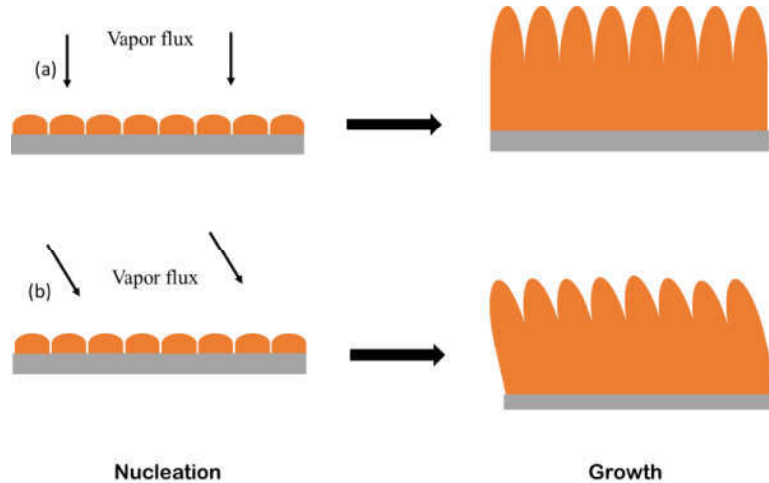


*Figure 3.6. (a) The normal incidence of the vapor flux that yields growth of a columnar microstructure in the direction of the substrate normal. (b) Growth of tilted columns due to a grazing incidence angle of the vapor flux.*

### 3.4. Characterization techniques

The prepared samples were studied employing several structural characterization techniques namely, electron microscopies such as scanning electron microscopy, transmission electron microscopy and x-ray scattering (x-ray reflectivity and x-ray diffraction). The optical properties were investigated by optical absorption spectroscopy and reflectivity measurements. On the other hand, low-temperature photoluminescence measurement was carried out and analyzed to study the emission property of the samples and to identify the defect states. Electrical characterizations of the fabricated devices were investigated through I-V measurements (with and without illumination). Brief discussions about these techniques are mentioned in the following subsections.

#### 3.4.1. Structural characterization techniques

##### 3.4.1.1. X-ray scattering

X-ray diffraction techniques have been extensively used as a non-destructive probe for the structural and interfacial study of thin-film and complex nanostructures such as superlattice, quantum dot, etc. with resolution down to one atomic layer. Although for a single epitaxial layer, the lattice constant, present of strain as well as the composition can be extracted directly from the experimental data, but for complex structures like superlattice, to extract various



parameters, simulation of the experimental data is necessary. In the grazing angle reflectivity regime, the scattered intensity profile depends only on the electron density distribution in the layer but does not depend on the crystal structure. It is sensitive to surface, interface roughness, inter-diffusion at the interfaces whereas, in the high angle diffraction region, the intensity profile is sensitive to the atomic arrangements in the crystal. So, information about the crystalline quality, difference in lattice constants at the interface, strain profile, the composition could be obtained from x-ray diffraction analysis.

#### 3.4.1.1.1. X-ray diffraction and grazing incidence x-ray diffraction technique

X-ray diffraction (XRD) is a routine characterization technique in the field of material science and condensed matter physics. It plays an extremely important role to determine the crystallinity, purity, and phase of the materials. Usually, in the laboratory, the x-ray is generated by a two steps process. The electrons are accelerated through a large potential difference to increase their energy. Then the high energetic electrons strike with a stationary or rotating solid metal target that produces x-rays. Generally, in laboratory Cu, Fe or Mo used as the metal target. X-ray of wavelength  $\lambda$  reflected from the periodic planes of atoms (Figure 3.7) constructively interfere according to Bragg's law

$$n\lambda = 2d_{hkl}\sin\theta \quad (3.8)$$

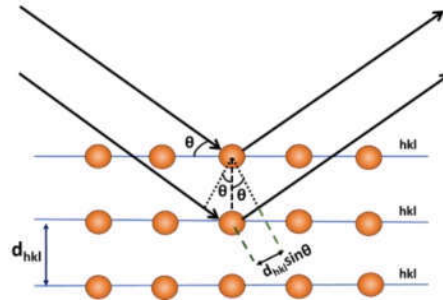
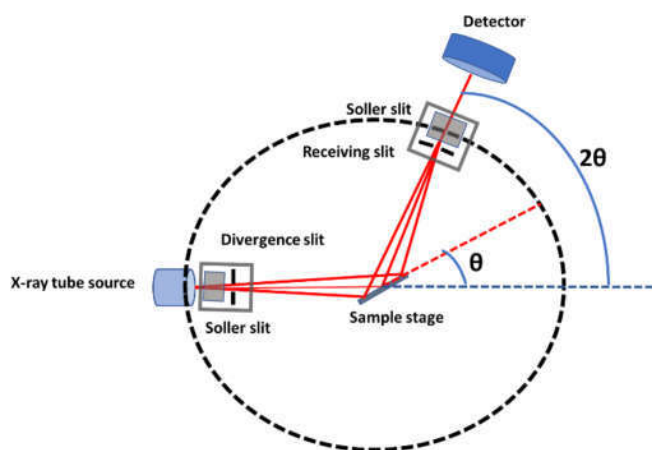


Figure 3.7. Bragg's representation for diffraction of X-ray from atomic planes.

where  $\lambda$  is the wavelength of the x-ray,  $d_{hkl}$  is the inter planer spacing between (hkl) planes,  $\theta$  is the angle of diffraction, and  $n$  is an integer which is called the order of diffraction. Materials with a tetragonal structure like  $\text{ZnSnP}_2$ , the inter-planner spacing can be expressed in terms of lattice parameter ( $a$ ,  $c$ ) as

$$d_{hkl}^2 = \frac{1}{\sqrt{\frac{h^2+k^2}{a^2} + \frac{l^2}{c^2}}} \quad (3.9)$$

The diffraction profile obtained by the XRD technique heavily depends on the periodicity of the sample. This technique is usually used to investigate the crystallographic orientation of the powder sample thus conventionally known as x-ray powder diffractometry. However, this technique is equally useful for polycrystalline specimens to find out the different crystallographic orientations present in the sample by comparing the experimental data with the available database provided by the International Center for Diffraction Data (ICDD) and Joint Committee on Powder diffraction standards (JCPDS). These results can even be utilized to calculate the average crystalline size of the samples. The main function of a diffractometer is to detect and record the intensity of x-ray coming from materials as a function of the angle of deviation ( $2\theta$ ). Figure. 3.8 depicts the geometrical arrangement of the x-ray source, specimen



*Figure 3.8. Arrangement of the x-ray source, sample, and detector in a typical lab-based setup for x-ray scattering measurements.*

and detector in a standard x-ray diffractometry instrument. In the laboratory-based diffractometer, relative movements among the x-ray tube, specimen, and the detector ensure the recording of diffraction intensity with  $2\theta$  ranging from  $5^\circ$ - $180^\circ$ . Note that the  $\theta$  angle is not the angle between the incident beam and the specimen surface. In case of symmetric scans, it is the angle between the incident beam and the crystallographic plane that generates diffraction as the planes parallel to the sample surface. In asymmetric scans, the planes of interest are not parallel to the surface.

The electromagnetic radiation emitted from the x-ray tube is collimated by passing through the Soller slits, which is basically a set of closely spaced thin metal plates parallel to the plane of incidence of x-ray. The beam coming out from the Soller slits is incident on the specimen. The specimen is usually in the form of a flat plate or pressed powder, placed on a stationary platform. The diffracted beam is taken through the receiving slits and monochromatic filter

before reach to the detector. Receiving filters collimate the diffracted beam whereas monochromatic filters suppress all background radiations and only allow  $K_\alpha$  line.

In a standard diffractometer, the sample holder remains stationary thus data can be recorded in different geometric configurations by individually controlling the motion of the source and the detector. There may be various scanning modes such as  $\theta$ - $2\theta$ ,  $\omega$ - $2\theta$ , etc depending on the relative arrangement of the source, sample, and detector. In the  $\theta$ - $2\theta$  scanning mode, the detector's angular displacement is twice that of the source in the same time interval. It must be noted that the plane of motion of the source and the detector is perpendicular to the surface of the sample. In  $\omega$ - $2\theta$  scan, however, the detector moves similar to the previous case but the source remains stationary. Generally, the  $\omega$ - $2\theta$  scan is preferred over  $\theta$ - $2\theta$  for the thin film having a thickness less than 100 nm. For  $\omega$  less than  $5^\circ$  the method is called grazing incidence x-ray diffraction (GIXRD).

#### **3.4.1.1.2. X-ray reflectivity measurements**

X-ray reflectivity (XRR) measurement has become an extremely powerful non-destructive characterization technique for probing the microstructure of the samples such as film-thickness, density, interface or surface roughness and inter-diffusion of layered structures. This technique becomes useful for thin films having a thickness below 400 nm where other methods like spectroscopic ellipsometry do not able to provide correct result. For the angle of incidence less than the critical angle of the sample-air interface, x-rays fail to penetrate the outer surface of the specimen owing to the total external reflection. X-ray starts to enter the sample when the angle of incidence becomes greater than the critical angle. The interference between the reflected x-rays coming from two distinct interfaces produces fringes (called kissieg fringes) which contains the information about the sample. This measurement is carried out in  $\theta$ - $2\theta$  scanning mode. The value of  $\theta$  starts from less than the critical angle and goes to the maximum where the intensity of the measured signal becomes equivalent to the existing background radiation. Typically, the variation of  $2\theta$  lies between  $0.2^\circ - 12^\circ$ . Figure. 3.8 demonstrates a typical geometrical arrangement of the x-ray source, specimen, and detector used in the laboratory for reflectivity measurements in  $\theta$ - $2\theta$  configuration.

#### **3.4.1.2. Electron microscopy**

The spatial resolution of an optical microscope is restricted to few microns owing to the diffraction limit of visible radiations. To investigate the surface and the atomic structure of materials with a higher resolution beyond the limit of an optical microscope is very crucial not

only to look into the insight of the material but also to understand its macroscopic properties. Electrons can be accelerated through high potential difference (100-300 keV) region to gain sufficient energy to possess wavelength well below that of light. This property makes them an eligible candidate for studying materials in the nanoscale regime.

#### 3.4.1.2.1. Scanning electron microscopy

From its inception, the scanning electron microscopy (SEM) has proven to be a powerful and popular tool for exploring the surface morphology at a sub-micron level. SEM's image resolution depends on the energy of the probing electrons and the method of interactions with the specimen. Since the emission efficiency of secondary electrons produces in this process is limited to the surface geometry, surface chemical characteristics and bulk chemical composition of the samples thus, it can provide information about the surface morphology and also the chemical composition. The SEM measurement unit is consisting of an electron gun as electrons source, a high electric field across the electrodes for rising the electronic energy, a system of electromagnetic lenses which focus the electron beam onto the sample, scanning coils for preciously controlling the position of the beam on the surface, the sample chamber and detectors that measure the signals originated by electron scattering from the specimen. During measurement, the chamber containing all the components is maintained to a high vacuum for preventing any unwanted scattering of the electrons. Figure. 3.9 is illustrating all the major components for the formation of the image in SEM. Conventionally, two types of electron sources are used, one based on the thermionic emission and the other, field emission. A thermionic electron gun relies on the emission of electrons from a filament due to heating. Usually, the tungsten filaments are used as the cathode considering its highest melting point and lowest vapor pressure among all available metals. On the other hand, in the case of the field emission, electrons quantum-mechanically tunnel through the existing energy barrier between the metal and air. Typically, the field emission gun consists of two anodes. The first anode (at  $\sim 0-5$  kV) delivers a sufficient electric field for tunneling of electrons from the tip, whereas the second one (at  $\sim 1-50$  kV) accelerates the electrons to enhance the energy before the striking. An electron of charge  $e$  is moving with a velocity  $\mathbf{u}$  in a magnetic field  $\mathbf{B}$ , will experience the Lorentz force  $\mathbf{F}$  given by:

$$\mathbf{F} = e \mathbf{u} \times \mathbf{B} \quad (3.10)$$

It must be noted that this force can only influence the trajectory of the electrons keeping their energy unchanged. The existing magnetic field in the SEM is highly non-uniform. The total

magnetic field of the electromagnetic lens system can be divided into two independent components the vertical axial component ( $H_z$ ) and the horizontal radial component ( $H_r$ ). The radial component causes the electron to move along  $z$ -direction following a helical trajectory with respect to the axis while the other one reduces the diameter of the helix. As a result, the

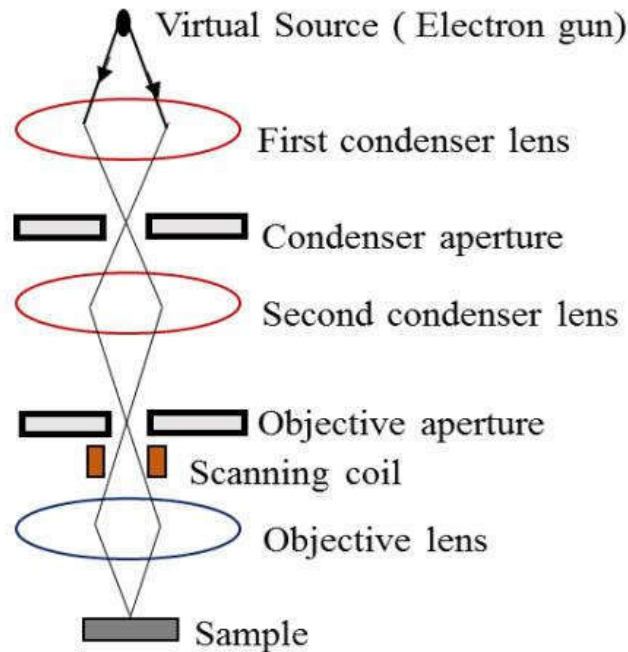


Figure 3.9. Schematic representation of the major components of a SEM instrument

electron beam spirals down the column as it passes through the electromagnetic lens and becomes finely focused on the sample for imaging purposes. Usually, there are two different lenses are placed in the SEM instrument, the condenser lens, and the objective lens. The first one basically focuses and guides the emitted electrons to travel through the SEM column. The objective lens focuses the electron beam onto the sample surface. The raster like scanning of

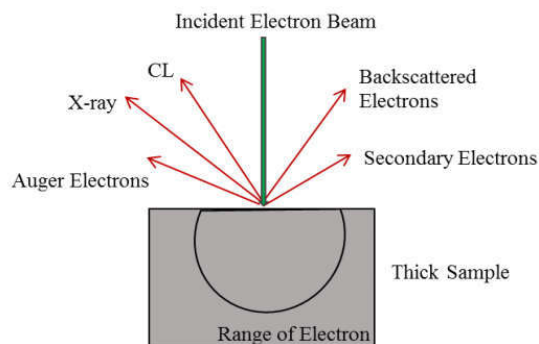


Figure 3.10. Detectable signals generated when an energetic electron beam is incident on the sample in SEM.

the electron beam over the surface of the sample is done by controlling the beam position by employing electric and magnetic field. Typically, a deflection coil consists of four radially oriented coils arranged so that the magnetic field is perpendicular to the axis of the system. The typical accelerating voltage used in the SEM is of the order of a few kilovolts.

When an energetic beam of electrons scanning over the sample surface, several phenomena such as the production of secondary electrons, backscattered electrons, Auger electrons, x-ray photon emission, and cathodoluminescence occur due to the interaction between the electrons and sample atoms. Among them, secondary electrons are the most abundant and frequently utilized to obtain the image of the surface in SEM. Figure. 3.10 illustrates the several phenomena which are usually observed when an energetic electron beam interacts with the sample. Energetic incident electrons can collide with the electrons in the sample and knock them out from their occupied position which is called secondary electrons. During the process, the incident electrons lose little energy and continue to generate more secondary electrons as they travel further into the sample. A single incident electron will typically generate a shower of thousands of secondary electrons (SE) until it stops. Since a large number of SE are generated, the detection of SE is the most common mode of operation for SEM sample imaging. Note that the SE have low energies so that SE generated deep in the sample are unable to travel to the surface and consequently unable to contribute to the formation of the image. So, the SE detected are primarily from the region close to the sample surface ( $<10$  nm). Hence SE imaging would produce good topographical/morphological information of the sample. The SEM generates an image of the sample by scanning the electrons over the sample surface while a SE detector placed near the sample collects the signal generated. In SEM, operating at a higher magnification means scanning the focused electron beam over a smaller area of the sample. Naturally, when the magnification reaches a high value, more effort is required to obtain a high-quality image. The quality of the image also depends on the type of sample being imaged too. The SEM requires a high vacuum environment in order to function properly. If a poor vacuum is maintained in the system, air molecules will damage the electron source. Moreover, the electron beam would also be scattered by the air molecules in the chamber. The collision between the electrons and the air molecules could give rise to ionization and discharge. Hence, the stability of the beam and the quality of the images would be affected. Additionally, the presence of air molecules in the SEM system can result in chemical reactions between the sample and the molecules. The result is the formation of some compound on the sample. This will affect the quality of the image too.

### 3.4.1.2.2. Field emission scanning electron microscopy

The working principle of a field emission scanning electron microscopy, abbreviated as FESEM, is almost identical to the usual SEM. The process of electron generation is the main distinguishing factor between these two techniques. In FESEM electrons are being produced by thermionic field emission while in SEM it is done by thermionic emission. The electron's quantum mechanically tunnels through a sharp metal tip in presence of an extremely high electric field. Thereafter, the emitted electrons are accelerated to increase energy and focused to form a narrow beam that scans the sample surface following a raster pattern that produces secondary electrons from every point of the sample. The detector identifies them and produces an equivalent electrical signal to form the surface topography.

### 3.4.1.2.3. Energy-dispersive x-ray spectroscopy

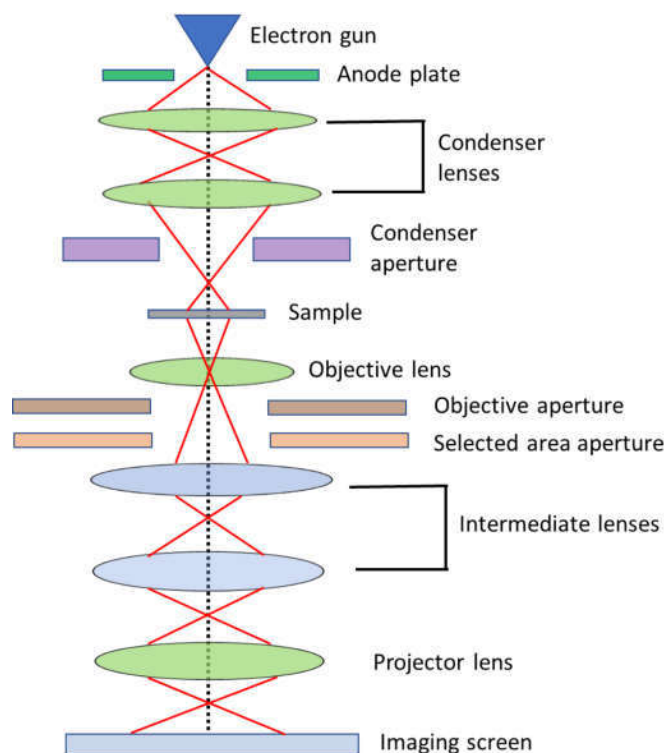


Figure 3.11. Schematic representation of TEM.

Energy-dispersive X-ray spectroscopy (EDX) is a characterization tool for roughly estimating the relative atomic concentration i.e. the elemental compositions in the sample. The time of scanning by a focused high energy electron beam, there is a finite probability of removing electrons from the inner shell of the atoms leading to a vacant state at those specific positions. The higher energy electrons from the outer orbital jump to fill up the vacant inner cell

producing emission of electromagnetic radiation. The transitions to the K-th shell produce x-ray which is detected and analyzed to extract the stoichiometric information of the specimen.

#### **3.4.1.2.4. Transmission electron microscope**

The invention of the high-resolution transmission electron microscope (HRTEM) has completely changed the way of visualizing the specimen in the nanometer realm. This technique is very powerful which can provide a variety of essential information such as crystallographic orientation, phase, defects in the structure, grain boundary, etc. The working of this type of microscope is limited to the wave property associated with the electrons. Its magnification power is even higher than SEM. In HRTEM the imaging of the ultrathin piece of the sample is obtained by passing the high energy ( $\sim 300$  keV) beam of electrons through it. Figure 3.11 represents the schematic structure of a typical HRTEM. The working principle of TEM is almost identical to the SEM. The electrons emitted from the electron gun by thermionic emission are energized by applying a very high potential difference of  $\sim 300$  KeV which is nearly one order of magnitude greater than that of SEM. Before the interaction with the sample, the electrons move through a region with a magnetic field that controls the diameter and the position of the beam. The transmitted beam is detected and amplified by three different lensing arrangement. Combining all these steps the final image is formed which is displayed in the monitor. Note that the HRTEM images provide information inside the sample, not the surface as obtained in SEM. TEM can be operated in two different modes (1) diffraction mode (2) imaging mode. Detection of elastically scattered electrons gives the diffraction patterns during the former mode operation whereas in the latter case, spatial intensity fluctuations are obtained by identifying the inelastically scattered electrons. The dark field image is obtained when the objective lens recognizes the diffracted electron beam. The operation of TEM requires an ultra-high vacuum and high voltage.

#### **3.4.1.2.5. Selected area electron diffraction**

Selected area electron diffraction (SAED) is an extremely helpful technique for obtaining the crystal structure of the measuring sample. The experimental measurement can only be carried out in a TEM. When a beam of the electrons is passing through the sample, diffraction takes place where the atoms behave like a diffraction grating. Thus, depending upon the sample's crystal structure a part of the incident electrons is scattered at a specific angle whereas the remaining fraction goes un-deviated. For single crystal, polycrystalline and amorphous



samples, the SAED pattern appears to be a series of properly ordered distinct spots, concentric circular ring and uniformly illuminated respectively.

#### 3.4.1.2.6. Bright field and dark field imaging

When a beam of electrons is incident on the sample, few of them scattered and the rest pass through without deflection. This un-deviated beam is called the direct beam. Detection of the scattered and un-scattered electrons results in the dark field (DF) and bright-field (BF) images, respectively. The chosen direct beam goes along the optic axis in the case of BF imaging while for DF imaging, the selected diffracted beam does not follow the direction of the optic axis which incorporates various aberrations during measurement. However, this hindrance can be

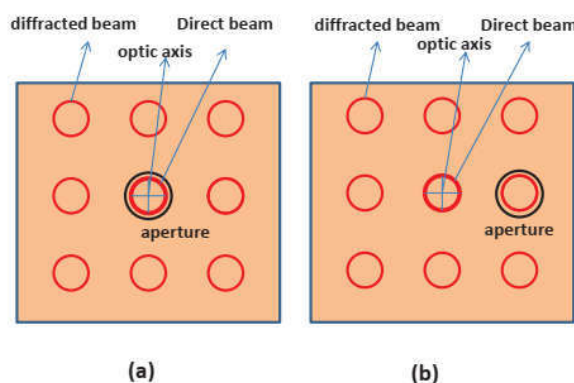


Figure 3.12. (a) Bright-field image (b) Darkfield image.

overcome by somehow aligning the beam with the optic axis. This is achieved by impinging the incident beam on the specimen at an angle equal and opposite to the selected scattered angle. Figure 3.12 shows the typically obtained DF and BF images.

#### 3.4.1.2.7. TEM specimen preparation

Undoubtedly, TEM is a powerful technique for microstructure and composition analysis, but it needs special attention for the specimen preparation. As the highly energized electrons have to be transmitted through the sample, so direct insertion of the sample in any form is not possible. The liquid sample can be inserted by drying them on the carbon-coated copper grid but the solid sample is to be made electron transparent following the steps described below.

##### 3.4.1.2.7.1. Initial thinning

The general lateral dimension of the specimen used for TEM is 3 mm in diameter. So a nearly about 3 mm diameter disc is cut from the sample using a disc grinder (Gatan). With the help of

a silicon carbide paper, they are thinned to the appropriate thickness for dimpling. Care should be taken such that no crack is introduced, otherwise, the sample will be broken at any of the later stages

#### **3.4.1.2.7.2. Dimpling**

After the initial thinning, the central portion of the sample is dimpled to reduce its thickness more. At the time of dimpling, as a small portion of the sample is made thinner, a chance for breaking of the sample is diminished. After that, the sample is placed on the turntable of the dimple grinder rotating at a constant speed. The grinding wheel is rotated orthogonally to the turntable rotation. Its speed can be varied according to the hardness of the sample. While dimpling, a diamond paste of grain size  $3\mu\text{m}$  is applied on the sample, dimple thickness was set and then the grinding wheel is lowered on the sample. After dimpling, the final polishing is done with a  $0.25\mu\text{m}$  grain size diamond paste.

#### **3.4.1.2.7.3. Ion milling**

The mechanical thinning as described previously is not enough to make the sample electron transparent. A Precession Ion Milling System (PIPS) (Gatan, Pleasanton, CA model) has been used for this purpose. In a PIPS, generally, Argon ions are impinged on the dimpled sample to knock out atoms from it to make it electron transparent. A CCD attachment in conjugation with an LCD is used to monitor the sample inside the chamber. In our present ion milling system, the energy of the ions can be varied up to 6 Kev and the angle of incidence can be varied up to  $\pm 10^\circ$ . The electron transparency of the sample is confirmed when a tiny perforation appears in the dimpled region, which can be viewed in the LCD.

#### **3.4.1.2.7.4. Sample preparation for cross-sectional TEM**

The cross-sectional view in TEM is necessary to extract the detailed structural parameters of epitaxial layers and other nanostructures. For the layers deposited on semiconductor substrates (Si, Ge, GaAs), at first two pieces of the sample of less than 3 mm width are cut and bonded with epoxy, keeping the deposited or the treated side face to face. For this purpose, Gatan Epoxy, which consists of two parts, a resin, and a hardener, is used. They are mixed in 8:1 (resin: hardener) ratio. After the epoxy is applied to the sample, it is heated at  $120^\circ\text{C}$  to get strong adhesion. Now the composite is inserted into a brass tube and the empty place is filled with thin dummy substrates and epoxy. The sample contained inside the brass tube is cut to make 0.5 mm discs, using a diamond wire saw. The disc is now mechanically thinned to 60-

100  $\mu\text{m}$  as described earlier, with the disc grinder and silicon carbide paper of different grit sizes. The central portion of this thin sample is now dimpled down to 30 $\mu\text{m}$  thickness and inserted inside the PIPS chamber for ion milling. After the ion milling, the electron transparent sample for the cross-sectional TEM (XTEM) study is obtained.

### 3.5. Optical characterization

#### 3.5.1. Optical absorption spectroscopy

UV-VIS-NIR absorption, transmittance, and reflectance measurements are simple and very effective for exploring the optical parameters ( $n$ ,  $k$ ) and bandgap of the semiconducting materials. Three phenomena viz, absorption, transmission, and reflection usually take place when light falls on any material. Spectrophotometer's working principle is effectively based on these three processes. An illustration of a typical spectrophotometer's different components is mentioned below (Figure 3.13).

- (i) **Light Source:** A single source is not sufficient to cover the entire range of the spectrum. So the unit usually contains a deuterium lamp that produces the UV radiation, a tungsten-halogen lamp for the visible and infrared portion of the electromagnetic spectrum.
- (ii) **Monochromator:** A monochromator selects a single wavelength of light coming out from the source and allows it to pass through.
- (iii) **Sample Holder:** A holder to keep the sample safely and steadily.
- (iv) **Integrating Sphere:** It is a hollow sphere which uniformly distributes the entered lights without absorbing them. Further details are given in the next subsection.
- (v) **Detector:** A photon detector usually made of a photomultiplier tube (PMT) or charge-coupled device (CCD) to sense the contribution of the sample on the incident radiation.
- (vi) **Computer:** A computer to control measurement procedures and record data. and helps to analyze and extract the optical parameters.

Directly measuring the wavelength-dependent absorption coefficient ( $\alpha(\lambda)$ ), also known as optical absorption spectra is a simple yet powerful technique for estimating the value of the bandgap. However, for opaque substrate, direct measurement of the absorption coefficient is not possible. Under those circumstances,  $\alpha(\lambda)$  is obtained by measuring the wavelength-

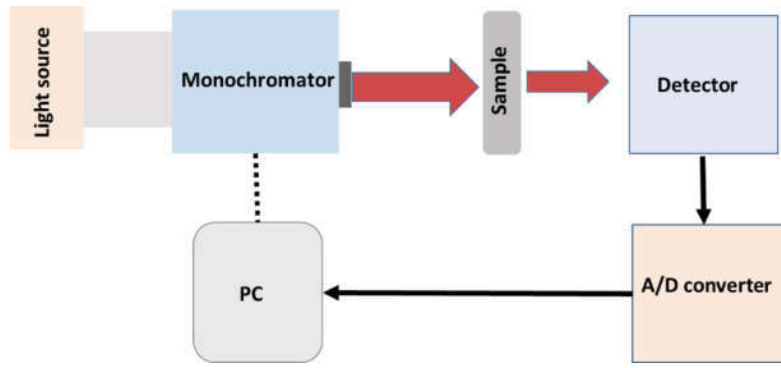


Figure 3.13. Schematic diagram of key components of a typical UV-vis spectrometer.

dependent transmittance ( $T(\lambda)$ ) and reflectance ( $R(\lambda)$ ) spectra and applying the mathematical equation connecting these three parameters [23] as written below

$$T(\lambda) = (100 - R(\lambda))^2 e^{-\alpha(\lambda)d} \quad (3.11)$$

Here,  $d$  signifies the film thickness. Both  $T$  and  $R$  appeared in the expression are in percentage. This equation does not include the contribution of multiple reflections taking place inside the film. It is worthwhile to mention that  $\alpha(\lambda)$ ,  $T(\lambda)$  and  $R(\lambda)$  do not depend on the intensity of the light emitted from the source. This technique is very essential and useful for determining the bandgap ( $E_g$ ) of the semiconducting thin film. The equation relating the bandgap and absorption coefficient of the semiconductor is given as follows [23]

$$\alpha h\nu = A(h\nu - E_g)^n \quad (3.12)$$

where  $A$  is a constant that does not depend on the energy of the incident radiation,  $h$  is the Plank constant and  $n$  is also a constant distinguishing the direct and indirect transitions i.e. type of the bandgap. The value of  $n$  is equal to  $\frac{1}{2}$  and  $2$ , for direct and indirect transitions, respectively. The bandgap of the sample can be estimated by extrapolating the linear region of  $(\alpha h\nu)^2$  vs  $h\nu$  plot to the  $h\nu$  axis (equation (2.5)) for direct transitions. Lamda 750 spectrophotometer in conjunction with an integrating sphere by Perkin Elmer was used to record all the transmittance and reflectance spectra. It is a dual beam spectrometer where the substrate is placed in the reference beam for removing its contribution from the output spectra.

### 3.5.2. Integrating sphere

An integrating sphere (also called the Ulbricht sphere) is a hollow spherical structure being coated with diffuse white materials of reflectance close to 100% on its inner wall (Figure 3.14). Furthermore, it contains two small openings one acts as an entrance while another one for exit. Compared to the dimension of the sphere, the size of the entrance and exit slits must be very

small. They are not placed diametrically opposite to each other. Light rays enter into the integrating sphere scatters several times and uniformly distributed while keeping the power conserved.

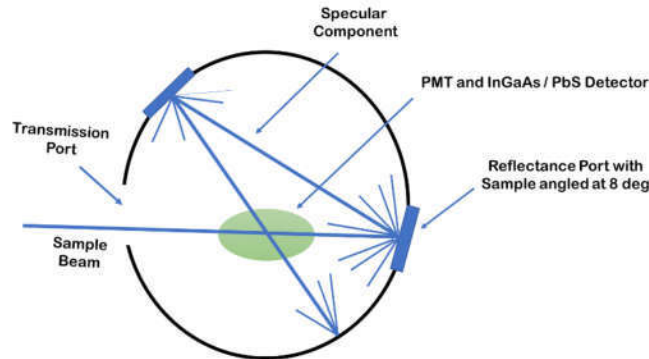


Figure 3.14. Pictorial representation of the setup of an integrating sphere.

### 3.5.3. Photoluminescence

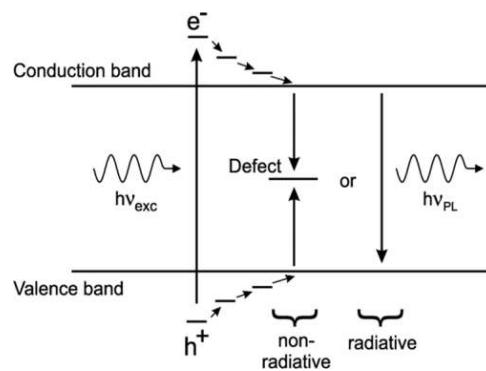


Figure 3.15. The involved mechanism in PL.

Photoluminescence (PL) is a process where an optically active material is excited by incident radiation from a laser source, typically having energy higher than the bandgap of the sample. The signals emitted by the samples due to different electronic transitions are investigated. The transitions can take place either directly from band-to-band or via different existing inter-band defect states as shown in Figure 3.15. Usually, this emission and absorption processes are instantaneous (time duration  $\sim$  few femtoseconds). However, imposing special conditions can extend this value to the order of a few minutes and even in a few hours. This technique becomes extremely helpful to find out bandgap, identify impurities and multiple recombination processes that are taking place.

Basically, PL is composed of three steps, which are given below.

1. Electron-hole pairs production by absorbing photon coming from the excitation source.

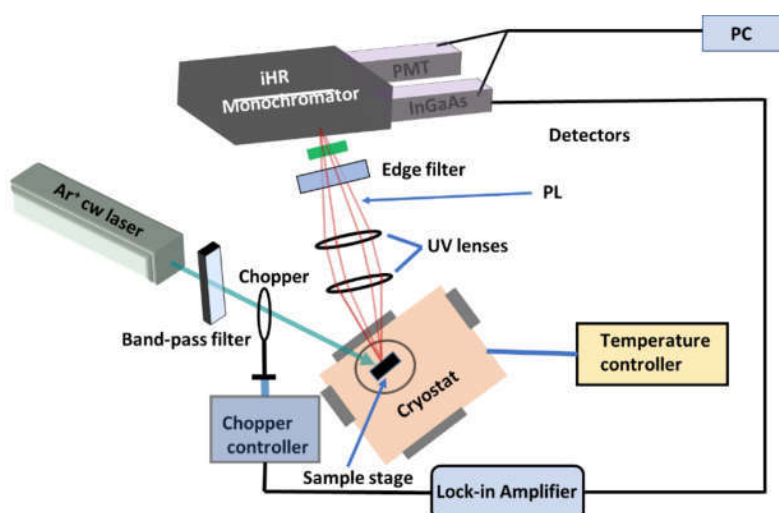


Figure 3.16. Schematic representation of PL experimental setup.

2. Radiative recombination of the electron-hole pairs generated in step 1.
3. Emission of electromagnetic radiation from the sample that originated in step 2.

### 3.5.3.1. Photoluminescence setup

The schematic representation of the experimental setup of PL is depicted in Figure 3.16 which is composed of the below mention apparatus-

1. **Excitation Source:** Melles Griot series argon-ion laser with tuneable excitation power from 13.65-70.90 mW with an operating wavelength of 514 nm was used as the excitation source. The laser beam is linearly polarized and the beam diameter is 1.79 mm.
2. **Band Pass Filter:** A band-pass filter with extremely narrow bandwidth is used. This eliminates all wavelengths except the laser line.
3. **Sample Platform:** A three-dimensional translatable platform with a holder for sample mounting.
4. **Collection Optics:** Two quartz lenses with 40 mm and 60 mm focal length were used to focus the PL emission to the monochromator generating from the sample
5. **Edge Filter:** A filter is used to block the laser line and its higher-order harmonics to reach the monochromator.
6. **Spectrometer:** Horiba Jobin Yvon iHR series spectrometer was used in our PL set up. iHR-550 spectrometer is automated triple grating spectrometers with a focal length of 550 mm (f/6.4 aperture) equipped with a PMT detector for the wavelength range of 185-900 nm and a cooled InGaAs detector with two-stage thermoelectric cooling for the range of 800-1700 nm. The spectral range of this spectrometer is 150 nm to 1500 nm with 1200 gr/mm grating

and resolution is 0.025 nm. The spectral range can be increased up to 40  $\mu\text{m}$  with additional gratings.

All the low-temperature PL measurements are carried out by a closed-cycle He cryostat, manufactured by Janis Research. Co. Inc., SHI- 4. The minimum achievable temperature in this cryostat is 4 k. The resulting luminescence is collected through a combination of two lenses coupled into a Horiba Jobin Yvon iHR-550 series spectrometer by which the luminescence is then spectrally dispersed. Thereafter, it is detected by the detector and recorded by the computer.

### 3.6. Photocurrent measurement

The current-voltage characteristics (I-V) were measured for the devices fabricated under dark as well as in the presence of light with variable wavelength to study the spectral dependency on the device performance. A schematic representation of the experimental setup involved in this measurement is shown in Figure 3.17. The different components are mentioned below

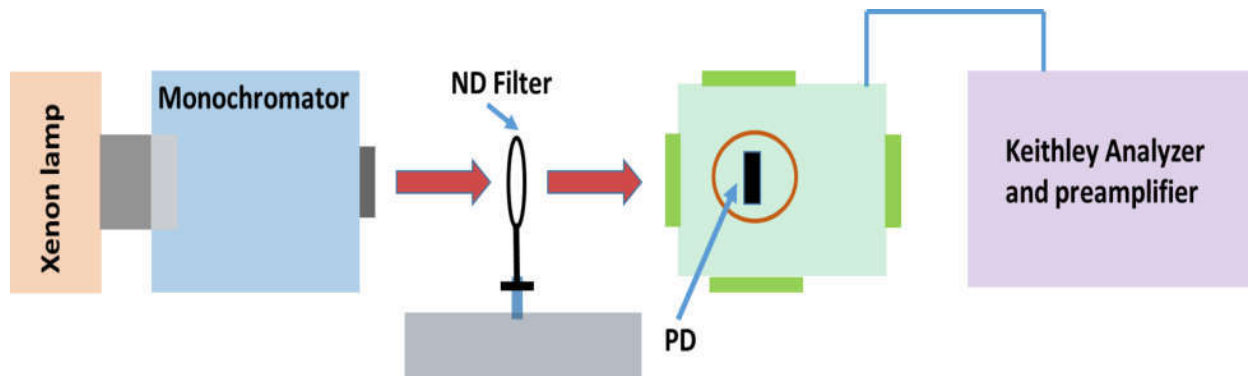


*Figure 3.17. Experimental arrangements of the spectral response measurement.*

**1. Excitation Source:** Horiba Jobin Yvon F11039/40 xenon lamp with an output power of 450 W was used as the excitation source. Its output spectra cover a spectral range from 150 nm to 1500 nm.

**2.Monochromator:** Gemini 180, double additive grating monochromator was used to disperse the radiation coming out from the xenon lamp. The radiation emitted from the monochromator illuminated the device.

**3. Neutral Density Filter:** It was placed between the sample and the monochromator to control the power of the light which is illuminating the sample.

**4. Sample Holder:** A three dimensional (X, Y, and Z) movable platform with a holder for mounting the sample.

**5. Source Meter:** The current-voltage (I-V) characteristics of the sample under dark and in presence of illumination were carried out by the keithley 4200 SCS.

### 3.7. Temporal measurement

The time response of a photodetector to switching frequency determines its capability to follow a fast-varying optical signal. In the work presented in this thesis, we have implemented two different methods for producing the pulsed signal to determine the speed of the PDs viz. (i) using chopper (ii) using a function generator. These methods have been discussed below in detail.

#### (i) Chopper Method:

The schematic of this arrangement is depicted in Figure 3.18. A chopper was powered with a function generator and placed in such a way that light emitted from the monochromator goes through the chopper before illuminating the sample. A digital storage oscilloscope (DSO) was connected across a resistance (Figure 3.18) for monitoring the periodic voltage fluctuation in the circuit. In the self-powered configuration, the DSO was directly connected across the PD.

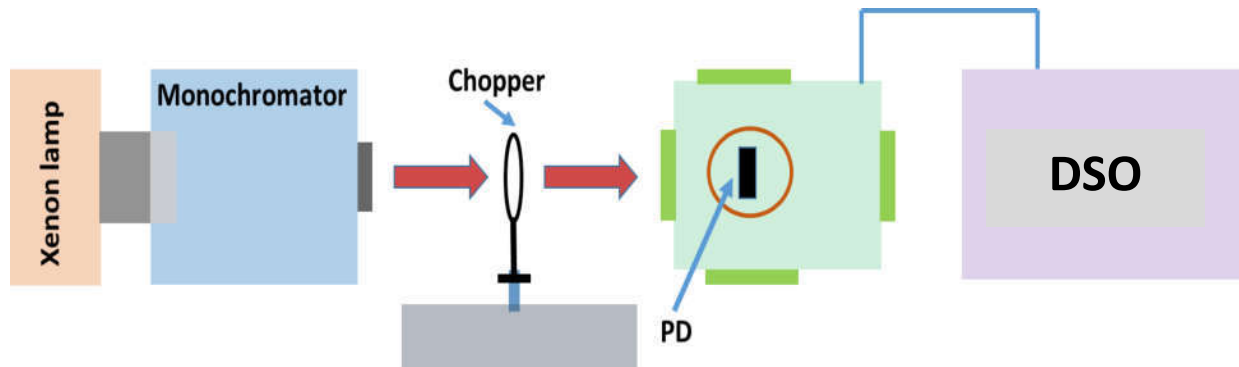


*Figure 3.18. Different components of the experimental setup of the temporal measurement.*

#### (ii) Function Generator Method:

Instead of chopping the light rays, samples were illuminated by a diode laser which was driven by a high-speed function generator to produce the square optical pulse with the desired frequency. The rest of the configuration remains unaltered. This configurational arrangement is represented in Figure 6.2 in chapter 6.

### 3.8. Physical vapour deposition



Physical vapor deposition (PVD) is basically different epitaxial techniques for thin film deposition in a vacuum environment. Thermal evaporation (TE), electron beam (e-beam) evaporation, sputtering, and ion implantation are the different PVD processes. This classification is effectively based on the method of evaporation. For TE the evaporation of the depositing material is accomplished by the resistive heating while the high energy e-beam assisted process is called e-beam evaporation. The entire growth process is basically divided into two steps which are mentioned below

- (i) First melting and then evaporation of the material to be deposited and
- (ii) Transportation of the vapor through the vacuum and nucleates on the substrate to form a layer.

The air pressure inside the chamber must be below  $10^{-5}$  mbar otherwise the film will be non-uniform.

### 3.8.1. Physical Vapour Deposition Setup

The different components of a PVD system are mentioned below. Figure 3.20 shows a schematic of the experimental arrangement.

**1. Vacuum Pump:** Two different types of vacuum pumps are used to reach the desired vacuum level of  $10^{-6}$  mbar. A turbo pump in conjugation with an oil pump (a rotary pump can also be used) is used to reach and sustain the required vacuum level for the deposition.

**2. Crucible:** The unit which contains the evaporant.

**3. Substrate Holder:** A metal plate is used for holding the substrate. This system is placed just above the crucible as represented in Figure 3.20.

**4. Heater:** A heater is connected with the sample holder for high-temperature deposition.

**5. Quartz Crystal Monitor:** This unit measures the thickness and the growth profile of the depositing materials. The frequency response of the quartz crystal with the coated material provides thickness information. The monitor must be calibrated by providing information like density and the acoustic impedance of the evaporant prior to the deposition.

**6. Current Controlling System:** The growth rate is varied by controlling the current in the circuit. High current signifies a faster growth rate.

**7. Electron Gun:** This section produces the electron beam for heating the evaporant.

or

**8. Filament:** This unit actually holds the materials and supplies heat for evaporation.

**9. Water Cooling System:** The crucible containing evaporent is cooled to prevent the spreading of the heating region.

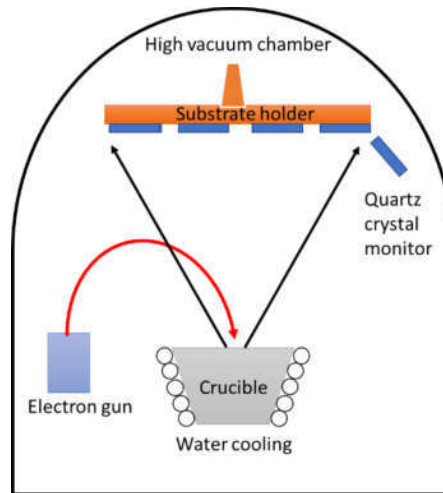


*Figure 3.20 Illustration of a typical PVD system.*

## References

- [1] T. Michely and J. Krug. Islands, mounds and atoms: Patterns and processes in crystal growth far from equilibrium. Springer, Berlin (2004).
- [2] R. Ditchfield and E. Seebauer. Phys. Rev. Lett. (1999), 82, 1185.
- [3] D. Adamovic, E. P. Münger, V. Chirita, L. Hultman, and J. E. Greene. Appl. Phys. Lett. (2005), 86, 211915.
- [4] X. W. Zhou and H.N.G. Wadley. Surf. Sci. (1999), 431, 42.
- [5] P. M. Martin. Handbook of deposition technologies for films and coatings. Elsevier Inc., Oxford, 3rd edition (2010).
- [6] P. Jensen and B. Niemeyer. Surf. Sci. (1997), 384, L823.
- [7] M. Ohring. Materials science of thin films. Academic Press, San Diego, 2<sup>nd</sup> edition (2002).
- [8] Z. Zhang and M. G. Lagally. Science, (1997), 276, 377.
- [9] F. A. Nichols and W. W. Mullins. J. Appl. Phys. (1965), 36, 1826.
- [10] G. Jeffers, M. A. Dubson, and P. M. Duxbury. J. Appl. Phys. (1994), 75, 5016.
- [11] J. Wen, S. Chang, J. Burnett, J. Evans, and P. Thiel. Phys. Rev. Lett. (1994), 73, 2591.
- [12] R. Hull and J. C. Bean. Principles and concepts of strained-layer epitaxy. In T. P. Pearsall (editor), Strained-layer superlattices: Materials science and technology Academic Press Inc., San Diego (1991).
- [13] Y. Zhao, Y. He, and C. Brown. Appl. Phys. Lett. (2012), 100, 033106.
- [14] K. Robbie, J. C. Sit, and M. J. Brett. J. Vac. Sci. Technol. B. (1998), 16, 1115.
- [15] M. Saraiva and D. Depla. J. Appl. Phys. (2012), 111, 104903.
- [16] J. M. García-Martín, R. Alvarez, P. Romero-Gomez, A. Cebollada, and A. Palmero. Appl. Phys. Lett. (2010), 97, 173103.
- [17] N. G. Nakhodkin and A. I. Shaldervan. Thin Solid Films (1972), 10, 109.
- [18] T. Hashimoto, K. Okamoto, K. Hara, M. Kamiya, and H. Fujiwara. Thin Solid Films (1982), 91, 145.

- [19] K. Okamoto, T. Hashimoto, K. Hara, M. Kamiya, and H. Fujiwara. Thin Solid Films, (1987) 147, 299.
- [20] K. Okamoto and K. Itoh. Jpn. J. Appl. Phys. (2005), 44, 1382–1388.
- [21] M. M. Hawkeye and M. J. Brett. J. Vac. Sci. Technol. A. (2007), 25, 1317.
- [22] J. Alami, P. O. A. Persson, D. Music, J. T. Gudmundsson, J. Bohlmark, and U. Helmersson. J. Vac. Sci. Technol. A. (2005), 23, 278.
- [23] S. Ebraheem, and A. El-Saied, Mater. Sci. Application, (2013), 4, 324.